

# The Heavy Photon Search Test Detector

M. Battaglieri<sup>a</sup>, S. Boyarinov<sup>b</sup>, S. Buelmann<sup>c</sup>, V. Burkert<sup>b</sup>, G. Charles<sup>d</sup>, W. Cooper<sup>e</sup>, N. Dashyan<sup>f</sup>, R. De Vita<sup>a</sup>, A. Deur<sup>b</sup>, R. Dupre<sup>d</sup>, H. Egiyan<sup>b</sup>, L. Elouadrhiri<sup>b</sup>, R. Essig<sup>g</sup>, V. Fadeyev<sup>h</sup>, C. Field<sup>i</sup>, A. Freyberger<sup>b</sup>, N. Gevorgyan<sup>f</sup>, F.-X. Girod<sup>b</sup>, N. Graf<sup>i</sup>, M. Graham<sup>i</sup>, K. Griffioen<sup>j</sup>, A. Grillo<sup>h</sup>, M. Guidal<sup>d</sup>, G. Haller<sup>i</sup>, P. Hansson Adrian<sup>i,\*</sup>, R. Herbst<sup>i</sup>, M. Holtrop<sup>k</sup>, J. Jaros<sup>i</sup>, S. K. Phillips<sup>k</sup>, M. Khandaker<sup>l</sup>, A. Kubarovskiy<sup>m</sup>, T. Maruyama<sup>i</sup>, J. McCormick<sup>i</sup>, K. Moffeit<sup>i</sup>, O. Moreno<sup>h</sup>, H. Neal<sup>i</sup>, T. Nelson<sup>i</sup>, S. Niccolai<sup>d</sup>, A. Odian<sup>i</sup>, M. Oriunno<sup>i</sup>, R. Paremuzyan<sup>f</sup>, E. Rauly<sup>d</sup>, E. Rindel<sup>d</sup>, P. Rosier<sup>d</sup>, C. Salgado<sup>l</sup>, P. Schuster<sup>n</sup>, Y. Sharabian<sup>b</sup>, K. Slifer<sup>k</sup>, D. Sokhan<sup>o</sup>, S. Stepanyan<sup>b</sup>, P. Stoler<sup>m</sup>, N. Toro<sup>n</sup>, S. Uemura<sup>i</sup>, M. Ungaro<sup>b</sup>, H. Voskanyan<sup>f</sup>, D. Walz<sup>i</sup>, L. B. Weinstein<sup>c</sup>, B. Wojtsekhowski<sup>b</sup>

<sup>a</sup>Istituto Nazionale di Fisica Nucleare, Sezione di Genova e Dipartimento di Fisica dell'Università, 16146 Genova, Italy

<sup>b</sup>Thomas Jefferson National Accelerator Facility, Newport News, Virginia 23606

<sup>c</sup>Old Dominion University, Norfolk, Virginia 23529

<sup>d</sup>Institut de Physique Nucléaire d'Orsay, IN2P3, BP 1, 91406 Orsay, France

<sup>e</sup>Fermi National Accelerator Laboratory, Batavia, IL 60510-5011

<sup>f</sup>Yerevan Physics Institute, 375036 Yerevan, Armenia

<sup>g</sup>Stony Brook University, Stony Brook, NY 11794-3800

<sup>h</sup>University of California, Santa Cruz, CA 95064

<sup>i</sup>SLAC National Accelerator Laboratory, Menlo Park, CA 94025

<sup>j</sup>The College of William and Mary, Department of Physics, Williamsburg, VA 23185

<sup>k</sup>University of New Hampshire, Department of Physics, Durham, NH 03824

<sup>l</sup>Norfolk State University, Norfolk, Virginia 23504

<sup>m</sup>Rensselaer Polytechnic Institute, Department of Physics, Troy, NY 12181

<sup>n</sup>Perimeter Institute, Ontario, Canada N2L 2Y5

<sup>o</sup>University of Glasgow, Glasgow, G12 8QQ, Scotland, UK

---

## Abstract

The Heavy Photon Search (HPS), an experiment to search for a hidden sector photon in fixed target electroproduction, is preparing for installation at the Thomas Jefferson National Accelerator Facility (JLab) in the Fall of 2014. As the first stage of this project, the HPS Test Run apparatus was constructed and operated in 2012 to demonstrate the experiment's technical feasibility and to confirm that the trigger rates and occupancies are as expected. This paper describes the HPS Test Run apparatus and readout electronics and its performance. In this setting, a heavy photon can be identified as a narrow peak in the  $e^+e^-$  invariant mass spectrum, above the trident background or as a narrow invariant mass peak with a decay vertex displaced from the production target, so charged particle tracking and vertexing are needed for its detection. In the HPS Test Run, charged particles are measured with a compact forward silicon microstrip tracker inside a dipole magnet. Electromagnetic showers are detected in a PbWO<sub>4</sub> crystal calorimeter situated behind the magnet used to trigger the experiment and identify electrons and positrons. Both detectors are placed close to the beam line and split top-bottom. This arrangement provides sensitivity to low-mass heavy photons, allows clear passage of the unscattered beam, and avoids the spray of degraded electrons coming from the target. The discrimination between prompt and displaced  $e^+e^-$  pairs requires the first layer of silicon sensors be placed only 10 cm downstream of the target. The expected signal is small, and the trident background huge, so the experiment requires very large statistics. Accordingly, the HPS Test Run utilizes high-rate readout and data acquisition electronics and a fast trigger to exploit the essentially 100% duty cycle of the CEBAF accelerator at JLab.

**Keywords:** silicon microstrip, tracking, vertexing, heavy photon, dark photon, hidden sector, electromagnetic calorimeter

---

\*Corresponding author.

Email address: phansson@slac.stanford.edu (P. Hansson)

Adrian)

**1** **Contents**

<b>2</b>	<b>1</b>	<b>Introduction</b>	<b>3</b>
<b>3</b>	<b>2</b>	<b>Detector Overview</b>	<b>3</b>
<b>4</b>	<b>3</b>	<b>The HPS Test Run Beamline</b>	<b>5</b>
<b>5</b>	<b>4</b>	<b>Silicon Vertex Tracker</b>	<b>5</b>
<b>6</b>	4.1	Layout . . . . .	6
<b>7</b>	4.2	Components . . . . .	7
<b>8</b>	4.3	Production, Assembly and Shipping . .	7
<b>9</b>	4.4	Alignment . . . . .	8
<b>10</b>	<b>5</b>	<b>Electromagnetic Calorimeter</b>	<b>8</b>
<b>11</b>	5.1	Components . . . . .	8
<b>12</b>	5.2	Layout . . . . .	8
<b>13</b>	5.3	Signal readout . . . . .	9
<b>14</b>	<b>6</b>	<b>Trigger and Data Acquisition</b>	<b>9</b>
<b>15</b>	6.1	Trigger system . . . . .	9
<b>16</b>	6.2	SVT Data Acquisition . . . . .	9
<b>17</b>	6.3	General Data Acquisition and Online Computing . . . . .	10
<b>19</b>	<b>7</b>	<b>Reconstruction and Performance</b>	<b>10</b>
<b>20</b>	7.1	SVT Performance . . . . .	10
<b>21</b>	7.1.1	Cluster and Hit Reconstruction .	11
<b>22</b>	7.1.2	Momentum and Vertexing Res- olution . . . . .	12
<b>23</b>	7.2	ECal Performance . . . . .	12
<b>24</b>	7.3	Trigger Performance . . . . .	13
<b>25</b>	7.4	Trigger Rate Comparisons . . . . .	14
<b>27</b>	<b>8</b>	<b>Summary and Outlook</b>	<b>14</b>
<b>28</b>	<b>9</b>	<b>Acknowledgements</b>	<b>15</b>

29     **1. Introduction**

30     The heavy photon ( $A'$ ), aka a “hidden sector” or  
31     “dark” photon, is a particle with mass  $10 - 1000 \text{ MeV}/c^2$   
32     which couples weakly to electric charge by mixing with  
33     the Standard Model photon [1]. Consequently, it can  
34     be radiated by electrons and subsequently decay into  
35      $e^+e^-$  pairs, albeit at rates far below those of QED trident  
36     processes. Heavy photons have been suggested by nu-  
37     merous beyond Standard Model theories [2], to explain  
38     the discrepancy between theory and experiment of the  
39     muon’s  $g - 2$  [3], and as a possible explanation of recent  
40     astrophysical anomalies [4, 5, 6]. Heavy photons couple  
41     directly to hidden sector particles with “dark” or “hid-  
42     den sector” charge; these particles could constitute all  
43     or some of the dark matter [7]. Current phenomenology  
44     highlights the  $20 - 1000 \text{ MeV}/c^2$  mass range, and sug-  
45     gests that the coupling to electric charge,  $\epsilon e$ , has  $\epsilon$  in the  
46     range of  $10^{-3} - 10^{-5}$ . This range of parameters makes  
47      $A'$  searches viable in medium energy fixed target elec-  
48     troproduction [8], but requires large data sets and good  
49     mass resolution to identify a small mass peak above the  
50     copious QED background. At small couplings,  $A'$  be-  
51     come long-lived, so detection of a displaced decay ver-  
52     tex can reject the prompt QED background and boost  
53     experimental sensitivity.

54     The HPS experiment [9] uses both invariant mass and  
55     secondary vertex signatures to search for  $A'$ . It uses a  
56      $\approx 1 \text{ m}$  long silicon tracking and vertexing detector in-  
57     side a dipole magnet to measure charged particle trajec-  
58     tories and a fast electromagnetic calorimeter just down-  
59     stream of the magnet to provide a trigger and identify  
60     electrons. The experiment utilizes very high-rate front-  
61     end electronics and runs at high trigger rates (up to  
62     50kHz), exploiting the 100% duty cycle of the JLab CE-  
63     BAF accelerator to accumulate the needed statistics.

64     The HPS Test Run, using a simplified version of the  
65     HPS apparatus, was proposed and approved at JLab as  
66     the first stage of HPS. Its purposes included demon-  
67     strating that the apparatus and data acquisition systems are  
68     technically feasible and the trigger rates and occupan-  
69     cies to be encountered in electron-beam running are as  
70     simulated. Given dedicated running time with electron  
71     beams, the HPS Test Run apparatus is capable of search-  
72     ing for heavy photons in unexplored regions of parame-  
73     ter space. The key design criteria for HPS and the HPS  
74     Test Run are the same:

- 75       • large and uniform acceptance in the forward region  
76       close to the beam in order to catch boosted  $A'$  de-  
77       cay products,
- 78       • beam passage through the apparatus in vacuum, to

79     eliminate direct interactions with the detector and  
80     minimize beam gas interactions,

- 81       • detector components that can survive and effi-  
82       ciently operate in a high radiation environment  
83       with local doses exceeding 100 Mrad.
- 84       • high-rate electronics with excellent timing resolu-  
85       tion to minimize out of time backgrounds,
- 86       • a flexible, redundant and efficient trigger selecting  
87       electron and positron pairs at rates up to 50 kHz,
- 88       • data handling rates of 100 MB/s to permanent stor-  
89       age,
- 90       • excellent track reconstruction efficiency for elec-  
91       trons and positrons,
- 92       • good angular and momentum resolution to recon-  
93       struct invariant mass precisely,
- 94       • excellent vertex resolution to discriminate dis-  
95       placed  $A'$  decays from prompt QED backgrounds,

96     The HPS Test Run apparatus was installed on April  
97     19, 2012, and ran parasitically in the photon beam of  
98     the HDice experiment [10] until May 18. The JLab  
99     run schedule precluded any dedicated electron beam  
100     running, but the HPS Test Run was allowed a short  
101     and valuable dedicated photon beam run at the end of  
102     scheduled CEBAF running. This final running provided  
103     enough data to demonstrate the functionality of the ap-  
104     paratus, document its performance, and explore trigger  
105     rates, as shown below.

106     This paper reviews the HPS Test Run apparatus, doc-  
107     umenting the performance of the trigger, data acqui-  
108     sition, silicon tracking detector, and the electromag-  
109     netic calorimeter at the level required for calculating the  
110     physics reach of the HPS experiment.

111     **2. Detector Overview**

112     The HPS Test Run apparatus was designed to run  
113     in Hall B at JLab using the CEBAF 499MHz electron  
114     beam at energies between 2.2 and 6.6 GeV and cur-  
115     rents between 200 and 600 nA. The overall design of  
116     the experiment follows from the kinematics of  $A'$  pro-  
117     duction which typically results in a final state particle  
118     within a few degrees of the incoming beam, especially  
119     at low  $m_{A'}$ . Detectors must therefore be placed close  
120     to the beam. The intense electron beam enlarges down-  
121     stream after multiple scattering in the target and elec-  
122     trons which have radiated in the target disperse horizon-  
123     tally in the field of the analyzing magnet. Together they

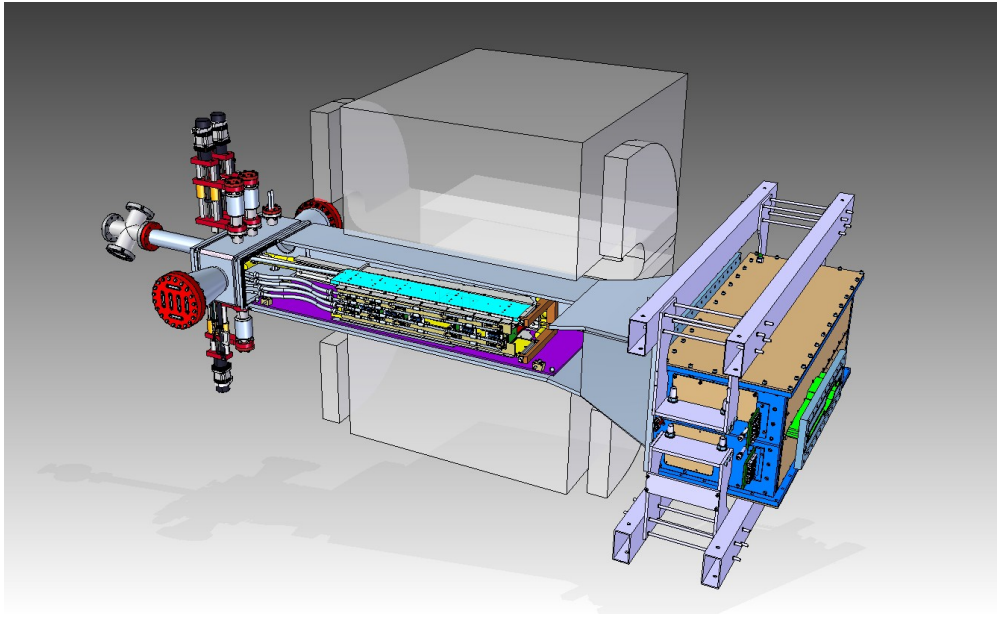


Figure 1: Rendering of the HPS Test Run apparatus installed on the beam line.

124 constitute a “wall of flame” which must be completely  
 125 avoided. Accordingly, the apparatus is split vertically  
 126 to avoid a “dead zone”, the region within  $\pm 15$  mrad of  
 127 the beam plane. In addition, the beam is transported in  
 128 vacuum through the tracker to minimize beam-gas inter-  
 129 action backgrounds. Even with these precautions, the  
 130 occupancies of sensors near the beam plane are high,  
 131 dominated by the multiple Coulomb scattering of the  
 132 primary beam, so high-rate detectors, a fast trigger, and  
 133 excellent time tagging are required to minimize their  
 134 impact. The trigger comes from a highly-segmented  
 135 lead-tungstate ( $\text{PbWO}_4$ ) crystal calorimeter located just  
 136 downstream of the dipole magnet.

137  
 138 A rendering of the apparatus installed on the beam line  
 139 is shown in Figure 1 and an overview of the coverage,  
 140 segmentation and performance is given in Table 1.

141 The silicon vertex tracking and vertexing detector for  
 142 the HPS Test Run, or SVT, resides in a vacuum cham-  
 143 ber inside the Pair Spectrometer (PS) dipole magnet in  
 144 Hall B at JLab. The magnetic field strength was 0.5 T  
 145 oriented vertically throughout the run. The SVT has  
 146 five measurement stations, or “layers,” beginning 10 cm  
 147 downstream of the target. Each layer comprises a pair  
 148 of closely-spaced silicon microstrip sensors responsi-  
 149 ble for measuring a single coordinate, or “view”. In-  
 150 troduction of a small (50 or 100 mrad) stereo angle

151 between the two sensors of each layer provides three-  
 152 dimensional tracking and vertexing throughout the ac-  
 153 ceptance of the detector. In order to accommodate the  
 154 dead zone, the SVT is built in two halves that are ap-  
 155 proximately mirror reflections of one another about the  
 156 plane of the nominal electron beam. Each layer in one  
 157 half is supported on a common support plate with inde-  
 158 pendent cooling and readout.

159  
 160 The electromagnetic calorimeter (ECal) is also split  
 161 into two halves. Each half of the ECal consists of  
 162 221  $\text{PbWO}_4$  crystals arranged in rectangular formation.  
 163 There are five rows with 46 modules in each row except  
 164 the row closest to the beam plane which has 37. The  
 165 light from each crystal is read out by an Avalanche Pho-  
 166 todioide (APD) glued on the back surface of the crys-  
 167 tal. Signals from the APDs are amplified using custom-  
 168 made amplifier boards before being sent to the data ac-  
 quisition electronics.

169 The Data Acquisition system combines two architec-  
 170 tures, the Advanced Telecom Communications Archi-  
 171 tecture (ATCA) based SVT readout system and VME-  
 172 bus Switched Serial (VXS) based digitization and trig-  
 173 gering system for the ECal. The system was designed  
 174 to run at up to 20 kHz trigger rate.

Table 1: Overview of the coverage, segmentation and performance of the HPS Test Run detector.

System	Coverage (mrad)	# channels	ADC (bit)	Time resolution (ns)	# layers	Segmentation	Performance
SVT	$15 < \theta_y < 70$ (5 hits)	12780	14	$\approx 2$ ns	5 (stereo layers)	$\approx 120 \mu\text{m} r - \phi$ $\approx 6 \mu\text{m} z$	$\sigma_{d0,y} \approx 100 \mu\text{m}$ $\sigma_{d0,x} \approx 300 \mu\text{m}$ $\sigma_{d0,z} \approx 1 \text{ mm}$
Ecal	$15 < \theta_y < 60$	442	12	4 ns	1	$1.33 \times 1.33 \text{ cm}^2$ $1.6 \times 1.6 \text{ cm}^2$	$\sigma(E)/E \approx 4.5\%$

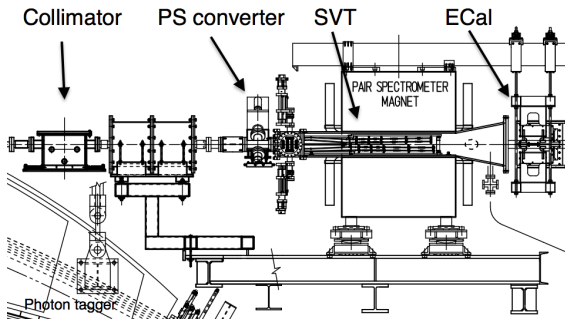


Figure 2: Layout of the HPS parasitic run.

### 3. The HPS Test Run Beamline

Since an electron beam was unavailable, the HPS Test Run detected the electrons and positrons produced by interactions of the secondary photon beam with a thin foil just upstream of the detectors. The HPS Test Run studied the performance of the detectors and the multiple coulomb scattering of the electrons and positrons. Figure 2 shows the layout of the setup on the beam line. The SVT was installed inside the Hall B pair spectrometer magnet vacuum chamber with the ECal mounted downstream of it. Both the SVT and the ECal were retracted off the beam plane compared to nominal electron beam running to allow clean passage of the photon beam through the system.

The photon beam was generated in the interaction of 5.5 GeV electrons with a  $10^{-4} X_0$  gold radiator located  $\approx 9$  m upstream of the PS. The primary beam and scattered electrons are deflected away from detectors by the dipole magnet of the photon tagging system. During the dedicated HPS Test Run period, the collimated (6.4 mm diameter) photon beam passes through the PS pair converter gold foil and later the HPS system as illustrated in Figure 3. The PS pair converter was located  $\approx 77$  cm upstream of the first layer of the SVT.

Data was taken on three different converter thicknesses with photon fluxes between 0.4 and  $1.3 \times 10^8/\text{s}$  at photon energies between 0.55 and 5.5 GeV produced by a 30 to 90 nA electron beam. Data was measured

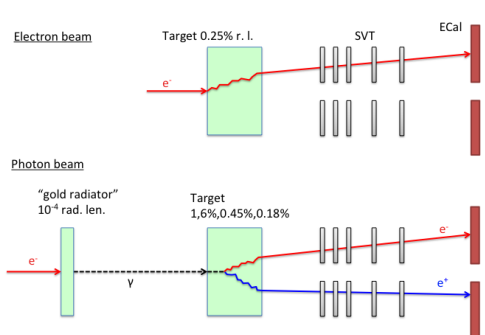


Figure 3: Illustrative comparison of HPS Test Run photon beam compared to the HPS electron beam.

Converter thickn. (% $X_0$ )	Duration (s)	$e^-$ on radiator ( $\mu\text{C}$ )
0	1279	88.1
0.18	2640	193.5
0.45	2149	140.7
1.6	911	24.4

Table 2: Measured integrated currents for the dedicated photon runs.

for both polarities of the PS dipole magnet.' The photon beam line during the HPS Test Run produced a relatively large number of  $e^+e^-$  pairs originating upstream of the converter position. This contribution was measured during data taking with "empty" converter runs, i.e. removing the converter but with all other conditions the same. The runs taken during the time dedicated to HPS Test Run is summarized in Table 2.

### 4. Silicon Vertex Tracker

The Silicon Vertex Tracker (SVT) enables efficient reconstruction of charged particles and precise determination of their trajectories. These measurements allow  $A'$  decays to be distinguished from background via simultaneous estimation of the invariant mass of  $e^+e^-$  de-

217 cay products and the position of decay vertexes downstream of the target.  
218

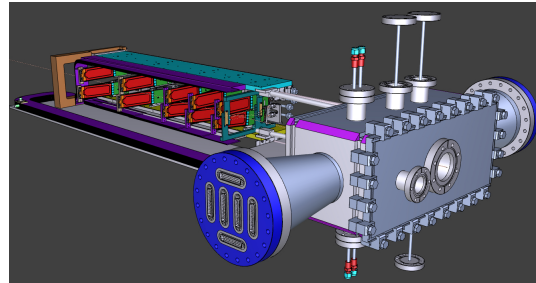
219 The design of the SVT is primarily driven by direct  
220 physics requirements and constraints from the environment  
221 at the interaction region. The A' decay products  
222 have momenta in the range of 1 GeV, so multiple scattering  
223 dominates mass and vertexing uncertainties for  
224 any possible material budget. The SVT must therefore  
225 minimize the amount of material in the tracking volume.  
226 The signal yield for long-lived A' is very small,  
227 so the rejection of prompt vertices must be exceedingly  
228 pure, on the order of  $10^{-7}$ , in order to eliminate all  
229 prompt backgrounds. To achieve the required vertexing  
230 performance the first layer of the SVT must be placed  
231 no more than about 10 cm downstream of the target.  
232 At that distance, it is found that the active region of  
233 a sensor can be placed as close as 1.5 mm from the  
234 center of the beam, defining the 15 mrad “dead zone”  
235 mentioned previously, to maximize low-mass A' ac-  
236 ceptance with decay products nearly collinear with the  
237 beam axis. At the edge of this “dead zone”, the radiation  
238 dose approaches  $10^{15}$  electrons/cm<sup>2</sup>/month, or roughly  
239  $3 \times 10^{14}$  1 MeV neutron equivalent/cm<sup>2</sup>/month [11], re-  
240 quiring the sensors to be actively cooled. Meanwhile,  
241 very low-energy delta rays from beam-gas interactions  
242 multiply the density of background hits, so the SVT  
243 must operate inside the beam vacuum. Finally, in or-  
244 der to protect the sensors, the detector must be movable  
245 so that it can be retracted during periods of uncertain  
246 beam conditions.

#### 247 4.1. Layout

248 The layout of the SVT is summarized in Table 4.1 and  
249 rendered in Figure 4. Each of the layers is comprised  
250 of a pair of closely-spaced silicon microstrip sensors  
251 mounted back-to-back to form a module. A 100 mrad  
252 stereo angle is used in the first three layers to provide  
253 higher-resolution 3D space points for vertexing. Using  
254 50 mrad in the last two layers breaks the tracking de-  
255 generacy of having five identical layers and minimizes  
256 fakes from ghost hits to improve pattern recognition.  
257 Altogether, the SVT has 20 sensors for a total of 12780  
258 readout channels.

Layer	1	2	3	4	5
<i>z</i> from target (cm)	10	20	30	50	70
Stereo angle (mrad)	100	100	100	50	50
Bend res. ( $\mu\text{m}$ )	$\approx 60$	$\approx 60$	$\approx 60$	$\approx 120$	$\approx 120$
Non-bend res. ( $\mu\text{m}$ )	$\approx 6$	$\approx 6$	$\approx 6$	$\approx 6$	$\approx 6$
# of sensors	4	4	4	4	4
Dead zone (mm)	$\pm 1.5$	$\pm 3.0$	$\pm 4.5$	$\pm 7.5$	$\pm 10.5$
Power cons. (W)	6.9	6.9	6.9	6.9	6.9

259 Table 3: Layout of the SVT.



260 Figure 4: A rendering of the SVT showing the modules on their  
261 support plates held by the hinged C-support on the left and the  
262 motion levers on the right. The sensors are shown in red and the  
263 hybrid readout boards in green. The beam enters from the  
264 right through a vacuum box with flanges for services.

265 The SVT is built in two separate halves that are mirror  
266 reflections of one another about the plane of the nom-  
267 inal electron beam. Each half consists of five modules  
268 mounted on a support plate that provides services to the  
269 modules and allows them to be moved as a group rel-  
270 ative to the dead zone. The two halves of the tracker  
271 are connected to hinges mounted on a C-shaped support  
272 just beyond the last layer that defines the nominal spac-  
273 ing between the upper and lower halves of the tracker.  
274 A shaft attached to each support plate in front of layer  
275 1 extends upstream and connects to a linear shift that  
276 transfers motion into the vacuum box through bellows  
277 to open and close the two halves around the dead zone.  
278 The C-support is mounted to an aluminum baseplate  
279 that defines the position of the SVT with respect to the  
280 vacuum chamber. Figure 5 shows a photograph of both  
281 completed detector halves prior to final assembly.



282 Figure 5: Both halves of the HPS Test Run SVT after final as-  
283 sembly at SLAC. The cooling manifolds and integrated cable  
284 runs are clearly seen.

278    4.2. Components

279    The sensors for the SVT are *p*-on-*n*, single sided,  
 280    AC coupled, polysilicon-biased microstrip sensors fab-  
 281    ricated on < 100 > silicon and have 30 (60)  $\mu\text{m}$  sense  
 282    (readout) pitch over their  $4 \times 10 \text{ cm}^2$  surface. This  
 283    sensor technology was selected to match the require-  
 284    ment of < 1%  $X_0$  per layer, single-hit resolution bet-  
 285    ter than 50  $\mu\text{m}$  and tolerance of a radiation dose of ap-  
 286    proximately  $1.5 \times 10^{14}$  1 MeV neutron equivalent/ $\text{cm}^2$   
 287    for a six month run. The sensors were purchased from  
 288    the Hamamatsu Photonics Corporation for the cancelled  
 289    Run 2b upgrade of the DØ experiment [12] which satis-  
 290    fied the requirement that the technology must be mature  
 291    and available within the time and budget constraints.

292    Despite having only small spots with very high occu-  
 293    pancy (up to 4 MHz/mm<sup>2</sup>) closest to the primary beam,  
 294    the rates are still high and lowering the peak occupancy  
 295    to approximately 1% for tracking requires a trigger win-  
 296    dows and hit time tagging of roughly 8 ns. The ECal  
 297    readout and trigger described in Sec. 5.3 can achieve  
 298    such resolution. To reach this performance the sen-  
 299    sors for the SVT are readout by the APV25 ASIC de-  
 300    veloped for the CMS experiment at CERN [13]. The  
 301    APV25 can capture successive samples of the shaper  
 302    output in groups of three at a sampling rate of approx-  
 303    imately 40 MHz. By fitting the known *CR-RC* shaping  
 304    curve to these samples, the initial time of the hit can  
 305    be determined to a precision of 2 ns for S/N  $\approx$  25 [14].  
 306    For electron beam running, six-sample readout and the  
 307    shortest possible shaping time (35 ns) is used to best  
 308    distinguish hits that overlap in time. The APV25 ASICs  
 309    are hosted on simple FR4 hybrid readout boards, out-  
 310    side the tracking volume, with a short twisted-pair pig-  
 311    tail cable to provide power and configuration and signal  
 312    readout. Along with a single sensor, these are glued  
 313    to a polyamide-laminated carbon fiber composite back-  
 314    ing making up a half-module. A window is machined  
 315    in the carbon fiber leaving only a frame around the pe-  
 316    riphery of the silicon to minimize material. A 50  $\mu\text{m}$   
 317    sheet of polyamide is laminated to the surface of the  
 318    carbon fiber with 1 mm overhang at all openings to en-  
 319    sure good isolation between the backside of the sensor,  
 320    carrying high-voltage bias, and the carbon fiber which  
 321    is held near ground.

322    The sensor modules for the SVT consist of a pair  
 323    of identical half-modules, sandwiched back-to-back  
 324    around an aluminum cooling block at one end and a sim-  
 325    ilar PEEK spacer block at the other. Figure 6 shows a  
 326    single module after assembly. The cooling block pro-  
 327    vides the primary mechanical support for the module as  
 328    well as cooling via copper tubes pressed into grooves

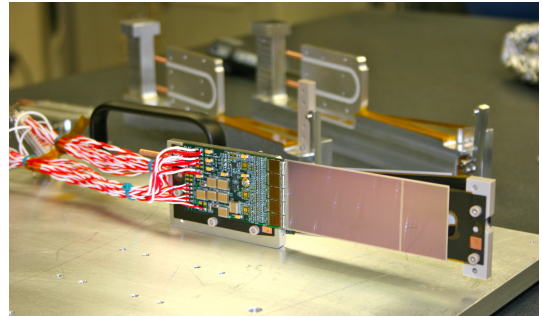


Figure 6: A prototype module assembly (foreground) with the 50 mrad (left) and 100 mrad (right) module assembly fixtures in the background. A pair of cooling blocks and a spacer block can be seen on the fixtures.

329    in the plates. The spacer block defines the spacing be-  
 330    tween the sensors at the far end of the module, stiffens  
 331    the module structure, and improves the stability of the  
 332    sensor alignment. The average support material in the  
 333    tracking volume is approximately 0.06%  $X_0$  per double-  
 334    sided module for a total material budget of 0.7% per  
 335    layer.

336    The total SVT power consumption budget of about  
 337    50 W is removed by a water/glycol mixture circulated  
 338    through a flexible manifold attached to the copper tubes  
 339    in the cooling blocks. During the HPS Test Run the  
 340    sensors were operated at around 23° C. The power con-  
 341    sumption is dominated by five APV25 ASICs on each  
 342    hybrid board consuming approximately 2 W, radiant  
 343    heat load is less than 0.5 W per sensor and leakage cur-  
 344    rent is only significant in a small spot after irradiation.

345    4.3. Production, Assembly and Shipping

346    Hybrids with APV25 ASICs underwent quick qualifi-  
 347    cation testing and each half-module was run at low tem-  
 348    perature ( $\approx$  5° C) and fully characterized for pedestals,  
 349    gains, noise and time response after assembly. Of 29  
 350    half-modules built, 28 passed qualification testing, leav-  
 351    ing 8 spare modules after completion of the SVT, all ca-  
 352    pable of 1000 V bias voltage without breakdown. Full-  
 353    module assembly and mechanical surveys were per-  
 354    formed at SLAC before final assembly, testing and ship-  
 355    ping of the SVT to JLab. A custom shipping container  
 356    with nested crates and redundant isolation for shock and  
 357    vibration was built in order to safely send the partly as-  
 358    sembled SVT to JLab. At JLab, the entire SVT was  
 359    integrated with the full DAQ and the power supplies be-  
 360    fore moving the module-loaded support plates to Hall B  
 361    for final mechanical assembly and installation inside of  
 362    the vacuum chamber.

363 **4.4. Alignment**

364 The SVT was aligned using a combination of optical,  
 365 laser and touch probe surveys at SLAC and JLab. The  
 366 optical survey of individual modules with a precision of  
 367 a few  $\mu\text{m}$  was combined with a touch-probe survey of  
 368 the overall SVT support structure, with 25-100  $\mu\text{m}$  pre-  
 369 cision, to locate the silicon sensor layers with respect  
 370 to the support plates and the mechanical survey balls  
 371 on the base plate. After full assembly and installation  
 372 of the SVT at JLab, a mechanical survey of the SVT  
 373 base plate position inside the pair spectrometer vacuum  
 374 chamber is used to determine the global position of the  
 375 SVT with respect to the CEBAF beam line. The re-  
 376 sulting survey-based alignment has the position of the  
 377 silicon sensors correct to within a few hundred microns  
 378 measured from tracks in the HPS Test Run data. A more  
 379 sophisticated global track-based alignment technique to  
 380 reach final alignment precision well below 50  $\mu\text{m}$  is be-  
 381 ing developed.

382 **5. Electromagnetic Calorimeter**

383 The electromagnetic calorimeter (ECal), installed  
 384 downstream of the PS dipole magnet, performs two es-  
 385 sential functions for the experiment: it provides a trigger  
 386 signal to select what events to read out from the detector  
 387 sub-systems and is used in the analysis to identify elec-  
 388 trons and positrons. The technology and design choices  
 389 are largely driven by the need for a compact forward de-  
 390 sign covering the SVT A' acceptance and able to fully  
 391 absorb electrons and positrons with energy between 0.5-  
 392 6.5 GeV, fine granularity and signal readout speed to  
 393 handle 1 MHz/cm<sup>2</sup> of electromagnetic background and  
 394 be radiation hard. The PbWO<sub>4</sub> crystal inner calorime-  
 395 ter of the CLAS detector [15], in operation since 2005  
 396 in Hall B, meets all the requirements set by HPS. The  
 397 modules from this calorimeter have been subsequently  
 398 repurposed for HPS.

399 **5.1. Components**

400 The ECal module shown in Figure 7 is based on a  
 401 tapered 160 mm long PbWO<sub>4</sub> crystal with a 13.3  $\times$   
 402 13.3 mm<sup>2</sup> (16  $\times$  16 mm<sup>2</sup>) front (rear) face wrapped in  
 403 VM2000 multilayer polymer mirror film. The scintilla-  
 404 tion light, approximately 3 photoelectrons/MeV, is read  
 405 out by a 5 $\times$ 5 mm<sup>2</sup> Hamamatsu S8664-55 Avalanche  
 406 Photodiode (APD) with 75% quantum efficiency glued  
 407 to the rear face surface using MeltMount 1.7 thermal  
 408 plastic adhesive. The low gain of APDs ( $\sim 200$ ) was  
 409 compensated with custom-made preamplifier boards,  
 410 which provide a factor of 2333 amplification of the APD  
 411 signal.

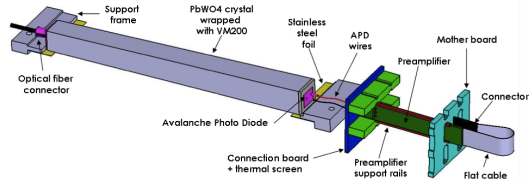


Figure 7: A schematic view of an ECal module.

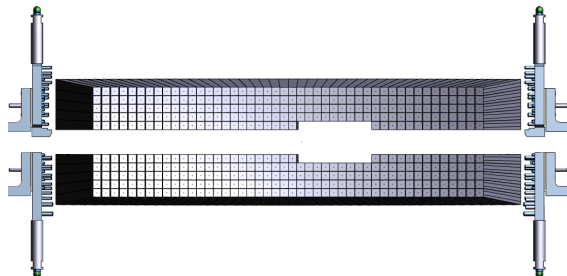


Figure 8: Rendered layout view of the ECal looking downstream.

412 **5.2. Layout**

413 Similar to the SVT, the ECal is built in two separate  
 414 halves that are mirror reflections of one another about  
 415 the plane of the nominal electron beam to avoid inter-  
 416 fering with the 15 mrad “dead zone”. As shown in  
 417 Figure 8, the 221 modules in each half, supported by  
 418 aluminum support frames, are arranged in rectangular  
 419 formation with 5 layers and 46 crystals/layer except for  
 420 the layer closest to the beam where 9 modules were re-  
 421 moved to allow a larger opening for the outgoing elec-  
 422 tron and photon beams. Each half was enclosed in a  
 423 temperature controlled box (< 1° F stability and < 4° F  
 424 uniformity) to stabilize the crystal light yield and the op-  
 425 eration of the APDs and its preamplifiers. Four printed  
 426 circuit boards mounted on the backplane penetrated the  
 427 enclosure and were used to supply the  $\pm 5$  V operating  
 428 voltage for the preamplifiers, 400 V bias voltage to the  
 429 APDs, and to read out signals from the APDs. Each half  
 430 of the ECal was divided into 12 bias voltage groups with  
 431 a gain uniformity of about 20%.

432 During the HPS Test Run, both halves were held in  
 433 place by four vertical bars attached to an above rail,  
 434 placing the front face of the crystals 147 cm from the  
 435 upstream edge of the magnet and with a 8.7 cm gap  
 436 between the innermost edge of the crystals in the two  
 437 halves.

438    **5.3. Signal readout**

439    After a 2:1 signal splitter, 1/3 of an amplified APD  
 440    signal was fed to a single channel of a JLab flash ADC  
 441    (FADC) board [16]. 2/3 of the signal was sent to a  
 442    discriminator module and then to a TDC for a timing  
 443    measurement. The FADC boards are high speed VXS  
 444    modules digitizing up to 16 APD signals at 250 MHz  
 445    and storing samples in 8  $\mu$ s deep pipelines with 12-bit  
 446    resolution. When a trigger is received, the part of the  
 447    pipeline from 5 samples before and 30 after the signal  
 448    which crossed a programmable threshold (for the HPS  
 449    Test Run this was set to  $\approx$  70 MeV) are summed and  
 450    stored in a 17-bit register for readout. In addition a  
 451    4 ns resolution timestamp of the threshold crossing is  
 452    reported in the readout for each pulse. This scheme  
 453    significantly compresses the data output of the FADC.  
 454    During offline data analysis, a calibrated pedestal value  
 455    is subtracted to obtain the actual summed energy. Two  
 456    20-slot VXS crates with 14 (13) FADC boards were em-  
 457    ployed in the HPS Test Run to read out the top (bottom)  
 458    half of the ECal. In the HPS Test Run 385 out of 442  
 459    modules (87%) were used in offline reconstruction, 39  
 460    modules were disabled or not read out (no FADC chan-  
 461    nel available, no APD bias voltage or masked out due  
 462    to excessive noise) and 18 were masked offline due to  
 463    noise.

464    **6. Trigger and Data Acquisition**

465    The DAQ system handles acquisition of data from the  
 466    ECal and SVT sub-detectors with two DAQ architec-  
 467    tures. The SVT DAQ is based on Advanced Telecom  
 468    Communications Architecture (ATCA) hardware while  
 469    the ECal uses VMEbus Switched Serial (VXS) based  
 470    hardware. Data from the sub-detectors are only read-  
 471    out when a trigger signal from the trigger system is re-  
 472    ceived.

473    **6.1. Trigger system**

474    The trigger system is designed to select time coinci-  
 475    dences of electromagnetic clusters in the top and bot-  
 476    tom halves of the ECal. Figure 9 shows a schematic  
 477    overview of each stage of the system. Each channel on  
 478    the FADC board has an independent data path to send 5-  
 479    bit pulse energy and 3-bit pulse arrival time informa-  
 480    tion every 32 ns to a trigger processing board (CTP), which  
 481    is in the same crate. The 3-bit pulse arrival time allows  
 482    the trigger to know the pulse timing at 4 ns resolution.  
 483    Contrary to the readout path described in Sec. 5.3, this  
 484    energy is a pedestal-subtracted time-over-threshold sum

485    with programmable offsets and minimum threshold dis-  
 486    criminator for each channel. With input from all FADC  
 487    channels, i.e. one half of the ECal, the CTP performs  
 488    cluster finding and calculates cluster energy and tim-  
 489    ing information. The 3x3 fixed-window, highly parallel,  
 490    FPGA-based cluster algorithm simultaneously searches  
 491    for up to 125 clusters with energy sum larger than the  
 492    programmable energy threshold ( $\approx$  270 MeV). Crystals  
 493    in the fixed-window are included in the sum if the lead-  
 494    ing edge of the pulse occurred within a 32 ns time win-  
 495    dow to take into account clock skew and jitter through-  
 496    out the system. The CTP only accepts clusters with the  
 497    highest energy 3x3 window locally to deal with over-  
 498    lapping and very large clusters. The sub-system board  
 499    (SSP) receives the clusters from the top and bottom half  
 500    CTP at a maximum of 250MHz and searches for pairs  
 501    of clusters in a 8 ns wide coincidence window. The SSP  
 502    sends triggers to the trigger supervisor (TS), which gen-  
 503    erates all the necessary signals and controls the entire  
 504    DAQ system readout through the trigger interface units  
 505    installed in every crate that participate in the readout  
 506    process.

507    The trigger system is free-running and driven by the  
 508    250 MHz global clock and has essentially zero dead  
 509    time at the occupancies expected for HPS. The trigger  
 510    supervisor can apply dead time if necessary, for exam-  
 511    ple on a ‘busy’ or ‘full’ condition from the front-end  
 512    electronics. The system is designed to handle trigger  
 513    rates above 50 kHz and has a latency set to  $\approx$  3  $\mu$ s to  
 514    match that required by the SVT APV25 ASIC. During  
 515    the HPS Test Run, for the most part the trigger system  
 516    required only a single cluster in either the top or bot-  
 517    tom Ecal halves and was tested to trigger rates above  
 518    100 kHz by lowering thresholds.

519    **6.2. SVT Data Acquisition**

520    The SVT DAQ is based on the Reconfigurable Clus-  
 521    ter Element (RCE) and cluster interconnect concept de-  
 522    veloped at SLAC as generic building blocks for DAQ



Figure 9: Block diagram of the ECAL trigger system consisting of the FADC that samples and digitizes signals for each detector channel and sends them for cluster finding in the CTP. The CTP clusters are sent to the SSP where the final trigger decision is taken based on pairs of clusters in both halves of the ECal. The decision is sent to the Trigger Supervisor (TS) that generates the necessary signals to readout the sub-detectors.



Figure 10: The SVT DAQ COB board with four data processing daughter cards (DPMs) visible on the left side.

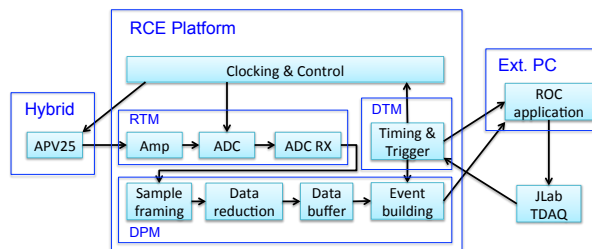


Figure 11: Block diagram overview of the SVT DAQ.

systems. The RCE is a generic computational building block, housed on a separate daughter card called Data Processing Module (DPM), that are realized on an ATCA front board called the Cluster On Board (COB), see Figure 10. The first generation RCE used in the HPS Test Run consisted of a Virtex 5 FPGA with 1 GB of DDR3 RAM. A schematic overview of the system is shown in Figure 11. The analog outputs of up to 12 SVT half-modules (60 APV25 ASICs) are digitized on the Rear-Transition-Module (RTM), a custom board on the back side of the ATCA crate, interfacing the HPS-specific readout to the generic DAQ components on the COB. A pre-amplifier converts the APV25 differential current output to a different voltage output scaled to the sensitive range of a 14-bit ADC operating at the system clock of 41.667 MHz. The RTM is organized into four sections with each section supporting three SVT half-module hybrids (15 APV25 ASICs). The RTM also includes a 4-channel fiber optic module and supporting logic which is used to interface to the JLab trigger system supervisor. Each section of the RTM is input to a DPM which applies thresholds for data reduction and organizes the sample data into UDP datagrams. The DPM also hosts an I<sup>2</sup>C controller used to configure and monitor the APV25 ASICs. A single ATCA crate with two COB cards was used, one supporting four DPMs

and one supporting 3 DPMs and one DPM that is configured as the trigger and data transmission module. The two COB cards and their DPMs are interconnected with a 10 Gb/s switch card [17] which also hosts two 1Gb/s Ethernet interfaces to the external SVT DAQ PC.

The external PC supports three network interfaces; two standard 1 Gb/s Ethernet and one custom low-latency data reception card. The first is used for slow control and monitoring of the 8 DPM modules and the second serves as the interface to the JLAB data acquisition system. The third custom low-latency network interface is used to receive data from the ATCA crate and supports a low latency, reliable TTL trigger acknowledge interface to the trigger DPM. This PC hosts the SVT control and monitoring software as well as the Read Out Controller application used to interface with the JLab DAQ.

In order to minimize cable length for the analog APV25 output signal the ATCA crate was located approximately 1 m from the beam line, next to our cable vacuum feed-troughs. Before shielding with lead-blankets was arranged, we observed two failures of normally reliable ATCA crate power supplies, time-correlated to beam instabilities.

Although trigger rates during the HPS Test Run were significantly lower, this system was tested at trigger rates up to 20 kHz and 50 MB/s.

### 6.3. General Data Acquisition and Online Computing

Every crate participating in the readout process contains a Readout Controller (ROC) that collects digitized information, processes it, and sends it on to the event builder. For the ECal, both VXS crates run ROC applications in a single blade Intel-based CPU module running CentOS Linux OS. For the SVT DAQ, the ROC application runs on the external PC under RHEL. The event builder assembles information from the ROCs into a single event which is passed to the event recorder that writes it to a RAID5-based data storage system capable of handling up to 100 MB/s. The event builder and other critical components run on multicore Intel-based multi-CPU servers. The DAQ network system is a network router providing 10 Gb/s high-speed connection to the JLab computing facility for long-term storage. For the HPS Test Run, both the SVT and ECal ROC had a 1 Gb/s link to the network router.

## 7. Reconstruction and Performance

### 7.1. SVT Performance

For the duration of the HPS Test Run all SVT modules and APV25 chips were configured to their nominal

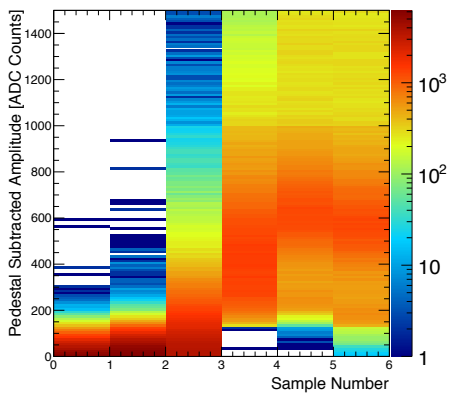


Figure 12: Accumulation of six pedestal-subtracted samples from individual SVT channels associated with hits on tracks.

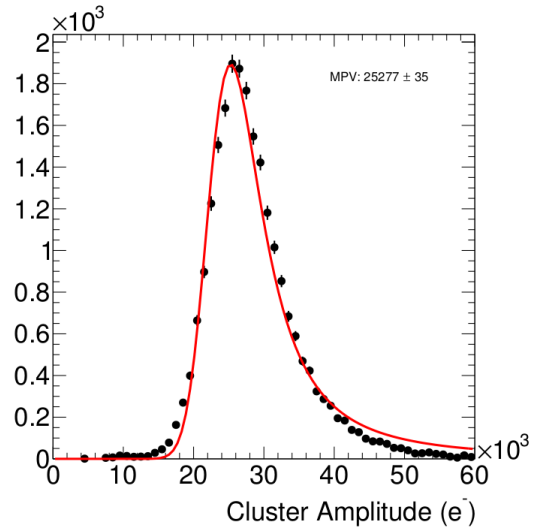


Figure 13: The cluster charge distribution for hits associated with track follow the characteristic Landau shape.

598 operating points [18] with all sensors reverse-biased at  
 599 180 V. The sensors were operated within a temperature  
 600 range of 20 – 24°C. Approximately 97% of the 12,780  
 601 SVT channels were found to be operating normally; the  
 602 fraction of dead or noisy channels varied from 2.4%  
 603 to 4.7% throughout the HPS Test Run. Most of these  
 604 losses were due to 2-4 misconfigured APV25 ASICs, a  
 605 known noisy half-module and problems in two particu-  
 606 lar APV25 ASICs.

### 607 7.1.1. Cluster and Hit Reconstruction

608 After a trigger is received, the amplitude of every  
 609 APV25 analogue output is sampled and digitized in  
 610 six consecutive time bins, separated by roughly 25 ns.  
 611 The typical, pedestal subtracted, pulse shape obtained  
 612 is shown in Figure 12. As the figure demonstrates, the  
 613 SVT was well timed-in to the trigger with the rise of the  
 614 pulse at the 3rd sampling point. In order to find the time,  
 615  $t_0$ , and amplitude of each hit, the six samples from each  
 616 channel are fitted to an ideal  $CR-RC$  function. Note that  
 617 in the HPS Test Run the APV25 ASICs were operating  
 618 with a 50 ns shaping time. These hits are passed through  
 619 a simple clustering algorithm which forms clusters by  
 620 grouping adjacent strips with the position of a cluster on  
 621 the sensor determined by the amplitude-weighted mean.  
 622 With a linear gain up to  $\approx 3$  MIPs, the cluster charge  
 623 for hits associated with a track follow the characteristic  
 624 Landau shape. A noise level between  $1.1 - 1.5 \times 10^3$   
 625 electrons was established through multiple calibration  
 626 runs giving a signal to noise ratio of 21 – 25. Lab-  
 627 based radioactive source tests were used to provide the  
 628 absolute charge normalization. After clustering hits on  
 629 a sensor, the hit time for each cluster is computed as

630 the amplitude-weighted average of the individually fit-  
 631 ted  $t_0$  on each channel. The  $t_0$  resolution is studied by  
 632 comparing the cluster hit time with the average of all  
 633 cluster hit times on the track shown in Figure 14. After  
 634 correcting for offsets from each sensor (time-of-flight  
 635 and clock phase) and accounting for the correlation be-  
 636 between the  $t_0$  and track time, the extracted  $t_0$  resolution is  
 637 2.6 ns. This is somewhat worse than the approximately  
 638 2 ns resolution expected for S/N 25 which we attribute  
 639 to the true pulse shape differing from our idealized fit  
 640 function which will be improved in the future. Reduc-  
 641 ing the APV25 ASIC pulse shaping time to 35 ns will  
 642 also improve time resolution. These results show that  
 643 we can operate with the six sample readout mode of the  
 644 APV25 chip and achieve time resolution adequate for  
 645 pileup rejection during electron running in HPS.

646 Good agreement was obtained between observed and  
 647 simulated occupancies after taking into account dead or  
 648 noisy channels. The hit reconstruction efficiency was  
 649 estimated by measuring the number of good tracks with  
 650 a hit close to the extrapolated intersection of a given  
 651 sensor that was excluded from the track fit itself. Tracks  
 652 which intersect regions with known bad channels or  
 653 very close to the edge region are excluded. The hit re-  
 654 construction efficiency, see Figure 15, was measured to  
 655 be above 98% and fairly uniform across the SVT.

656 The spatial resolution of similar microstrip sensors is  
 657 well established by test beam data, against which the  
 658 charge deposition model in the simulation is validated.  
 659 This resolution can be parameterized as a function of the

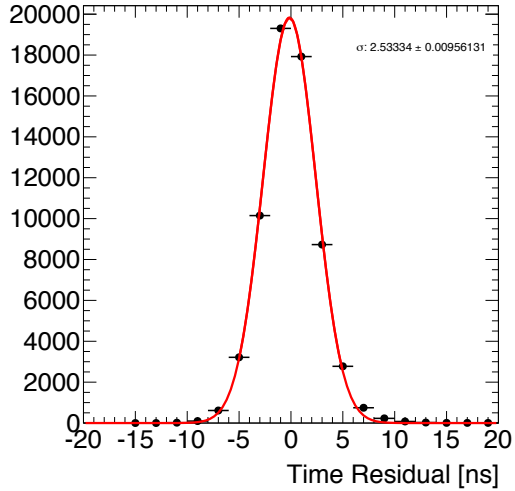


Figure 14: The residual of individual cluster times with the average of all clusters on the track.

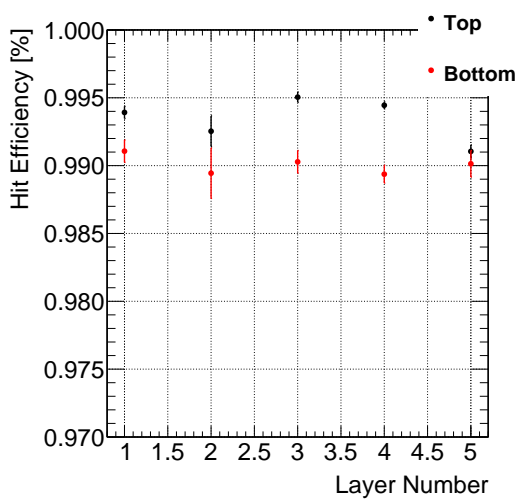


Figure 15: The hit reconstruction efficiency as a function of detector layer.

total signal to single-strip noise and the crossing angle of tracks through the sensor. The single-hit resolution for charged particles with signal to noise ratio above 20, as demonstrated here, is relatively constant at approximately 6  $\mu\text{m}$  for tracks that enter approximately normal to the sensors as in HPS.

#### 7.1.2. Momentum and Vertexing Resolution

By selecting  $e^+e^-$  pairs from the triggered events we are able to study basic distributions of pair production kinematics. Pairs of oppositely charged tracks, one in the top and one in the bottom half of the SVT, with momentum larger than 400 MeV were selected. The pair production kinematics are relatively well reproduced as shown in Figure 16.

The expected momentum resolution from simulation is between 4-5% for tracks in the momentum range of the HPS Test Run. By comparing the shapes of the kinematic distributions for single- and two track events between data and simulation we estimate an agreement with the nominal scale and resolution to within 10%.

In the HPS Test Run, as well as in electron running with HPS, the dominant source of uncertainty in the tracking and vertexing is multiple Coulomb scattering. For the vertexing performance the foremost difference compared to electron beam running is that the target was located approximately 67 cm upstream from our nominal target position; giving almost collinear tracks in the detector. The increased lever arm over which tracks are extrapolated widens the resolution with up to a factor of eight (depending on momentum) compared to what is achieved at the nominal electron target position for HPS. Figure 17 shows the horizontal and vertical positions of the extrapolated track at the converter position. While residual alignments show small shifts, the good agreement between data and simulated events of the widths indicates a good understanding of the material budget and distribution in the SVT. Having the dominant contribution to the vertex resolution approximately right demonstrates that the resolution in HPS, with a target at 10 cm, will be as calculated.

#### 7.2. ECal Performance

The integrated pulse of each FADC channel was converted to energy by subtracting a pedestal and applying a conversion factor to convert ADC counts to energy. The pedestals are measured using special runs where each trigger records 100 samples of signals from the APDs with 4 ns between each sample. The pedestals

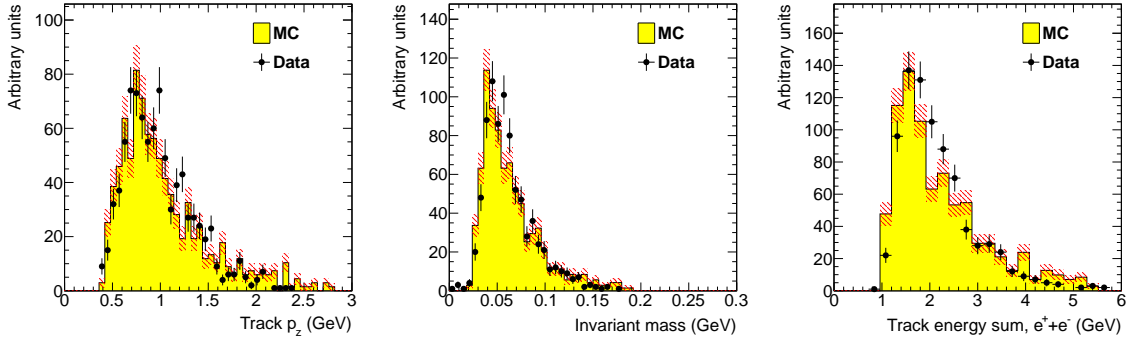


Figure 16: Kinematic distributions for  $e^+e^-$  pairs selected by opposite charged tracks in the top and bottom half of the tracker: track momentum in the top half of the SVT (left), invariant mass (middle) and the sum of the track momentum for the pair (right).

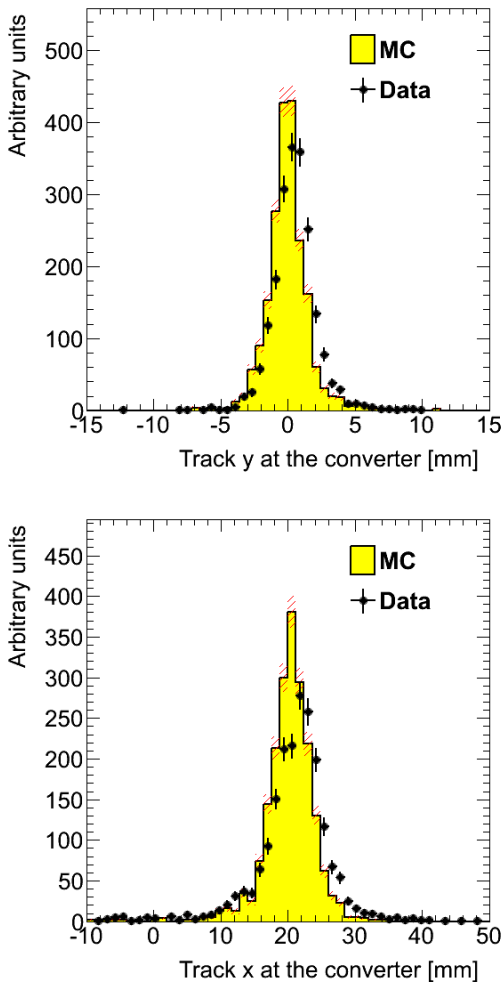


Figure 17: Vertical (top) and horizontal (bottom) extrapolated track position at the converter taking into account the measured fringe field.

were extracted from the part of the window before the actual hit in the calorimeter. Modules with signal above the threshold are clustered using a simple algorithm similar to the one deployed for the trigger (see Sec. 6.1). Due to the high effective readout threshold of 73 MeV the average number of crystals in a cluster was  $\sim 3$  and the simple clustering algorithm worked well for reconstruction of the detected shower energy. An average noise level of approximately 15 MeV was measured in special pedestal runs.

The ratio of the ECal cluster energy  $E$  to the momentum  $p$  of a matched track in the SVT was used to determine the conversion factors from ADC counts to energy. To compare data and simulation, all inoperable or noisy channels in the SVT and ECal were disabled in both data and simulation so that any efficiency or bias that affect the data should be reflected in the simulation. Iteratively, conversion coefficients for each crystal were adjusted until the  $E/p$  ratio in data and simulation were similar. The distribution of the  $E/p$  ratio in data and simulation are compared in Figure 18. The peak position of the distribution indicates the sampling fraction of the ECal, the fraction of the incident particle energy measured in the cluster. The width and tails of the distribution in data indicates imperfect calibration and noise of the ECal modules. This level of calibration and the agreement with simulation was found to be sufficient to study normalized event rates in the HPS Test Run.

### 7.3. Trigger Performance

As described above in Sec. 6, the energy from each crystal is measured differently in the trigger and what is readout from the ECal. The trigger performance was studied by simulating the trigger for each event and comparing to how the events were actually triggered. To eliminate trigger bias, we use a tag and probe

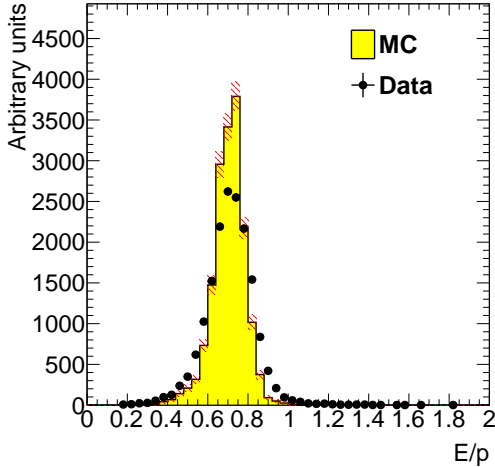


Figure 18: The ECal energy over track momentum ratio ( $E/p$ ) comparing data and simulation for single cluster triggers in the top half of the ECal.

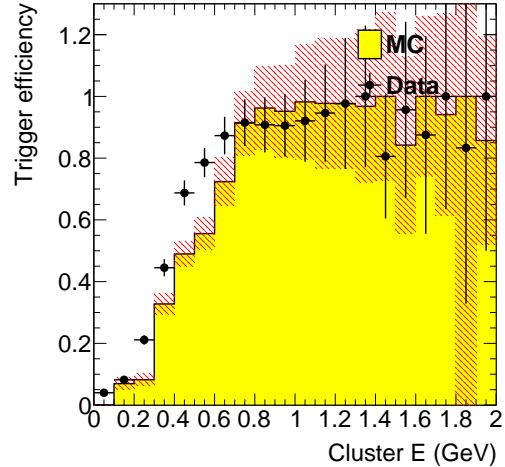


Figure 19: Trigger efficiency in both halves of the ECal for data and simulation as a function of cluster energy.

method: to study the trigger performance in one half of the ECal, we select events which triggered the other half and where there was exactly one probe cluster in the ECal half under study. We then measure trigger efficiency as the fraction of tagged events that fired the trigger in the probe half as a function of the probe cluster energy, shown in Figure 19. The trigger turn-on is slow and reaches an uneven plateau just below 1 GeV for two reasons; gain variations between different crystals lead to the threshold variations and the nonlinearity of the time-over-threshold integral means that the effective threshold is higher for clusters that span multiple crystals. The effective trigger threshold is therefore dependent on position and energy of the particle as well as cluster multiplicity.

As a cross-check we simulate the FADC trigger path by converting from readout hits (with fixed-size window integration) to trigger hits (time-over-threshold integration). The CTP clustering algorithm and the trigger decision from the SSP are simulated before we compare the trigger decision and trigger time to what was reported by the actual trigger. For every event, the trigger reports the trigger decision as a bit mask (top half, bottom half or both) and the time the trigger fired. The turn-on from the trigger threshold was measured to be 1280 in units of ADC counts as expected. The threshold was not perfectly sharp because of uncertainties in the conversion from readout to trigger hits described above, but based on comparisons with simulation we found that the trigger worked exactly as specified.

Converter (% $X_0$ )	<b>1.60</b>	<b>0.45</b>	<b>0.18</b>
EGS5	$1162 \pm 112$	$255 \pm 28$	$94 \pm 17$
GEANT4	$2633 \pm 250$	$371 \pm 38$	$114 \pm 18$
Observed	$1064 \pm 2$	$196 \pm 1$	$92 \pm 1$

Table 4: Observed and predicted event rate (in Hz) normalized to 90 nA for three different converter thicknesses. The uncertainty on the prediction includes systematic uncertainties from ECal alignment, background normalization, beam current normalization and limited statistics in the simulation.

#### 7.4. Trigger Rate Comparisons

Trigger rates observed in the HPS Test Run are dominated by multiple Coulomb scattered  $e^+e^-$  pairs in the converter. In simulated events, the rate of triggers depend on the modeling of the pairs angular distribution and the subsequent multiple Coulomb scattering in the converter. Rates from different converter thicknesses are used to study the varying multiple Coulomb scattering contribution (pair production angle is constant). Restricting clusters to a well calibrated region of the ECal and subtracting the “no converter” background we see agreement with the rates predicted by the EGS5 simulation program, see Table 7.4. This gives further confidence that the dominant source of background occupancy for HPS, multiple Coulomb scattered beam electrons, is well described [19, 20, 21].

## 8. Summary and Outlook

The HPS Test Run experiment, using a simplified version of the apparatus planned for the full HPS ex-

periment in a parasitic photon beam, demonstrated the feasibility of the detector technologies proposed for the silicon vertex tracker, electromagnetic calorimeter, and data acquisition systems. Performance from each of these subsystems has been shown to be adequate to conduct the full experiment successfully. Studies of multiple Coulomb scattering tails of electrons and positrons from photon conversions further backs expectations from simulation, giving credence to estimates of the detector backgrounds expected in electron beam running for HPS.

## 9. Acknowledgements

The authors are grateful for the support from Hall B at JLab and especially the Hall B engineering group for support during installation and decommissioning. They also would like to commend the CEBAF personnel for good beam performance, especially the last few hours of operating CEBAF6. The tremendous support from home institutions and supporting staff also needs praise from the authors.

This work has been supported by the US Department of Energy.

## References

- [1] B. Holdom, Two U(1)'s and Epsilon Charge Shifts, Phys.Lett. B166 (1986) 196.
- [2] R. Essig, J. A. Jaros, W. Wester, P. H. Adrian, S. Andreas, et al., Dark Sectors and New, Light, Weakly-Coupled Particles (2013).
- [3] M. Pospelov, Secluded U(1) below the weak scale, Phys.Rev. D80 (2009) 095002.
- [4] O. Adriani, et al. (PAMELA Collaboration), An anomalous positron abundance in cosmic rays with energies 1.5-100 GeV, Nature 458 (2009) 607–609.
- [5] M. Ackermann, et al. (Fermi LAT Collaboration), Measurement of separate cosmic-ray electron and positron spectra with the Fermi Large Area Telescope, Phys.Rev.Lett. 108 (2012) 011103.
- [6] M. Aguilar, et al. (AMS Collaboration), First Result from the Alpha Magnetic Spectrometer on the International Space Station: Precision Measurement of the Positron Fraction in Primary Cosmic Rays of 0.5350 GeV, Phys.Rev.Lett. 110 (2013) 141102.
- [7] N. Arkani-Hamed, D. P. Finkbeiner, T. R. Slatyer, N. Weiner, A Theory of Dark Matter, Phys.Rev. D79 (2009) 015014.
- [8] J. D. Bjorken, R. Essig, P. Schuster, N. Toro, New Fixed-Target Experiments to Search for Dark Gauge Forces, Phys.Rev. D80 (2009) 075018.
- [9] A. G. et al. (HPS Collaboration), HPS Heavy Photon Search Proposal, 2010.
- [10] A. Sandorfi, et al., 2012. URL: [http://www.jlab.org/exp\\_prog/proposals/06/PR-06-101.pdf](http://www.jlab.org/exp_prog/proposals/06/PR-06-101.pdf).
- [11] I. Rashevskaya, S. Bettarini, G. Rizzo, L. Bosisio, S. Dittongo, et al., Radiation damage of silicon structures with electrons of 900-MeV, Nucl.Instrum.Meth. A485 (2002) 126–132.
- [12] D. S. Denisov, S. Soldner-Rembold, D0 Run IIB Silicon Detector Upgrade: Technical Design Report (2001).
- [13] M. French, L. Jones, Q. Morrissey, A. Neviani, R. Turchetta, et al., Design and results from the APV25, a deep sub-micron CMOS front-end chip for the CMS tracker, Nucl.Instrum.Meth. A466 (2001) 359–365.
- [14] M. Friedl, C. Irmel, M. Pernicka, Readout of silicon strip detectors with position and timing information, Nucl.Instrum.Meth. A598 (2009) 82–83.
- [15] A. Radyushkin, P. Stoler (Eds.), Inner Calorimeter in Clas/dvcs Experiment, 2008.
- [16] D. H., et al., Integrated tests of a high speed VXS switch card and 250 MSPS flash ADCs, 2007. doi:10.1109/NSSMIC.2007.4436457.
- [17] R. Larsen, Emerging New Electronics Standards for Physics, Conf.Proc. C110904 (2011) 1981–1985.
- [18] L. Jones, APV25-S1: User guide version 2.2, RAL Microelectronics Design Group, 2011.
- [19] D. Attwood, P. Bell, S. Bull, T. McMahon, J. Wilson, et al., The scattering of muons in low Z materials, Nucl.Instrum.Meth. B251 (2006) 41–55.
- [20] G. Shen, C. Ankenbrandt, M. Atac, R. M. Brown, S. Ecklund, et al., Measurement of Multiple Scattering at 50-GeV/c to 200-GeV/c, Phys.Rev. D20 (1979) 1584.
- [21] B. Gottschalk, A. Koehler, R. Schneider, J. Sisterson, M. Wagner, Multiple coulomb scattering of 160 mev protons, Nuclear Instruments and Methods in Physics Research Section B: Beam Interactions with Materials and Atoms 74 (1993) 467 – 490.